1 **Atg39 links and deforms the outer and inner nuclear membranes in selective**

2 **autophagy of the nucleus**

3

4 Keisuke Mochida[1,2], Toshifumi Otani[1], Yuto Katsumata[1], Hiromi Kirisako[1], Chika Kakuta[1],

5 Tetsuya Kotani[1], Hitoshi Nakatogawa[1,*]

6

7 [1]School of Life Science and Technology, Tokyo Institute of Technology, Yokohama, Japan

8 *Correspondence to Hitoshi Nakatogawa: hnakatogawa@bio.titech.ac.jp

9

10 [2]Present address: Laboratory for Protein Conformation Diseases, RIKEN Center for Brain

11 Science, Wako, Japan

12

13

14 Condensed title: Atg39 deforms the nuclear envelope in nucleophagy

15

16

17   **Abstract**

18   In selective autophagy of the nucleus (hereafter nucleophagy), nucleus-derived double membrane

19   vesicles (NDVs) are formed, sequestered within autophagosomes, and delivered to lysosomes or

20   vacuoles for degradation. In *Saccharomyces cerevisiae*, the nuclear envelope (NE) protein Atg39

21   acts as a nucleophagy receptor, which interacts with Atg8 to target NDVs to forming

22   autophagosomal membranes. In this study, we revealed that Atg39 is anchored to the outer nuclear

23   membrane (ONM) via its transmembrane domain and also associated with the inner nuclear

24   membrane (INM) via membrane-binding amphipathic helices (APHs) in its perinuclear space

25   region, thereby linking these membranes. We also revealed that overaccumulation of Atg39

26   causes the NE to protrude towards the cytoplasm, and the tips of the protrusions are pinched off

27   to generate NDVs. The APHs of Atg39 are crucial for Atg39 assembly in the NE and subsequent

28   NE protrusion. These findings suggest that the nucleophagy receptor Atg39 plays pivotal roles in

29   NE deformation during the generation of NDVs to be degraded by nucleophagy.

Introduction

Macroautophagy (hereafter autophagy) is the mechanism whereby cellular material such as proteins and RNA as well as larger structures such as protein aggregates, phase-separated liquid droplets, and membrane-bound organelles are degraded, playing an important role in the maintenance and regulation of various cellular functions (Nakatogawa, 2020; Morishita and Mizushima, 2019). Autophagy initiates with the formation and expansion of the membrane cisterna known as the isolation membrane or phagophore, which bends, becomes spherical, and seals to sequester degradation targets within the resulting double membrane vesicle, the autophagosome. The autophagosome then fuses with the lysosome in animals and the vacuole in yeast and plants for degradation of the sequestered material within these lytic organelles. Sequestration of cellular components into autophagosomes proceeds in both a selective and non-selective manner. In selective types of autophagy (hereafter selective autophagy), autophagy receptors bind to degradation targets and act to recruit core Atg proteins, which mediate autophagosome biogenesis, to the targets for their efficient sequestration into the autophagosomes (Morishita and Mizushima, 2019; Farré and Subramani, 2016). Previous studies suggest that different organelles, including mitochondria, peroxisomes, the endoplasmic reticulum (ER), and the nucleus, are degraded by selective autophagy, and autophagy receptors responsible for degradation of these organelles have also been identified (Morishita and Mizushima, 2019; Farré and Subramani, 2016).

The nucleus contains chromosomes, and the double membraned nuclear envelope (NE) separates specific reactions such as DNA replication and gene transcription from the cytoplasm. The outer nuclear membrane (ONM) and the perinuclear space (NE lumen) are continuous with the membrane and the lumen of the ER, respectively, and therefore, these membranes and spaces share many proteins. The ubiquitin-proteasome system is vital in preventing the accumulation of

54 aberrant proteins in the nucleus. However, nuclear inclusion bodies are formed when these

55 proteins accumulate beyond the capacity of the system in neurodegenerative diseases such as

56 Huntington's disease (Enam et al., 2018; Woulfe, 2008). Recent studies suggest that nuclear

57 components are delivered to and degraded in lysosomes or vacuoles via autophagy (Mijaljica and

58 Devenish, 2013; Mochida et al., 2015). In the budding yeast *Saccharomyces cerevisiae*, we

59 identified the transmembrane protein Atg39 as a receptor for selective autophagy of the nucleus

60 (hereafter nucleophagy) (Mochida et al., 2015). Meanwhile, yeast cells lacking Atg39 exhibited

61 abnormal nuclear morphology and an early cell death phenotype under nitrogen starvation. We

62 and other groups also reported selective autophagy of nuclear pore complexes and nuclear lamina

63 in yeast and mammalian cells, respectively (Dou et al., 2015; Tomioka et al., 2020; Lee et al.,

64 2020). These results therefore suggest that selective degradation of nuclear components via

65 autophagy also has a significant impact on nuclear homeostasis in cells.

66   We previously revealed that when *S. cerevisiae* cells are subjected to nitrogen starvation

67 or treated with the Tor kinase complex 1 (TORC1) inhibitor rapamycin, Atg39 is expressed and

68 localized to the NE, and, as with other autophagy receptors (Farré and Subramani, 2016), it

69 interacts with Atg11, which serves as a scaffold to recruit core Atg proteins, and Atg8, which is

70 located on expanding isolation membranes, loading nucleus-derived double membrane vesicles

71 (NDVs) of ~200 nm into the autophagosomes (Mochida et al., 2015). The outer and inner

72 membranes of NDVs are derived from the ONM and inner nuclear membrane (INM), respectively,

73 with nucleoplasmic and nucleolar proteins existing in the vesicle lumen. To generate NDVs, the

74 ONM and INM need to induce deformation and fission in a coordinated manner. Because NDVs

75 do not accumulate in the cytoplasm of cells deficient for autophagosome formation, these vesicles

76 are thought to form concomitantly with autophagosome formation. We also found that Atg39

77 accumulates in the NE at contact with the site of autophagosome formation; however, the

78   mechanisms underlying these processes of NDV formation during nucleophagy remain unknown.

79   In this study, we discovered that Atg39 binds to both the ONM and INM via its N-

80   terminal transmembrane domain and C-terminal amphipathic helices (APHs), respectively,

81   thereby linking these membranes. We also found that overexpression of Atg39 drives the

82   formation of protrusions from the NE accompanied by both the ONM and INM. The APHs in the

83   C-terminal perinuclear space region of Atg39 play multiple roles in nucleophagy: Atg39 retention

84   to the NE; the basal and enhanced assembly of Atg39 in the NE, the latter of which occurs in

85   conjunction with autophagosome formation; and the formation of NE protrusions, the tips of

86   which are pinched off to generate NDVs.

87

88   **Results**

89   **Atg39 is an ONM protein**

90   Although Atg39 was predicted to be an integral membrane protein with a single transmembrane

91   domain, separating it into N-terminal (1–144) and C-terminal (165–398) regions, its membrane

92   topology has yet to be demonstrated experimentally. To determine the membrane topology of

93   Atg39, lysates were prepared from yeast cells expressing Atg39 N- and C-terminally tagged with

94   HA and GFP sequences, respectively, were treated with proteinase K in the presence or absence

95   of the detergent Triton X-100 (TX-100) (Fig. 1A and B). Immunoblotting using anti-HA antibody

96   showed that the HA tag in HA-Atg39-GFP was digested by proteinase K regardless of the

97   presence of TX-100 (Fig. 1A). In contrast, immunoblotting with anti-GFP antibody revealed that

98   the GFP tag in Atg39-GFP was largely resistant to proteinase K in the absence of TX-100,

99   although it was trimmed to a size corresponding to the protein lacking the region N-terminal to

100   the transmembrane domain (Fig. 1B). These results suggest that Atg39 is a single-pass membrane

101   protein with N- and C-terminal regions exposed to the cytoplasm and the perinuclear space,

102   respectively (Fig. 1C), consistent with the existence of Atg8- and Atg11-binding sequences in the

103   N-terminal region (Mochida et al., 2015).

104   To investigate whether Atg39 is embedded in the ONM only or in both the ONM and

105   INM, we used a split-GFP-based system (Smoyer et al., 2016). In this system, an N-terminal

106   sequence of GFP containing 10 β strands (GFP$^{1-10}$) was attached to the ONM/ER membrane

107   protein Scs2 (GFP$^{1-10}$-mCherry-Scs2) or the nucleoplasmic protein Pus1 (GFP$^{1-10}$-mCherry-Pus1),

108   and the remaining C-terminal sequence containing the last β strand of GFP (GFP^{11}) was fused to

109   the N terminus of Atg39 (GFP^{11}-Atg39) (Fig. 1D). When the two GFP fragments exist in the same

110   compartment, they form a functional GFP. GFP fluorescence was observed in the NE of cells

111   coexpressing GFP$^{1-10}$-mCherry-Scs2 and GFP^{11}-Atg39, but not those expressing GFP$^{1-10}$-

112   mCherry-Pus1 instead of GFP$^{1-10}$-mCherry-Scs2. When GFP$^{1-10}$-mCherry-Pus1 was coexpressed

113   with GFP^{11} fused to the INM protein Heh1 (also known as Src1), GFP fluorescence was observed

114   in the NE (INM), confirming that GFP$^{1-10}$-mCherry-Pus1 can form a functional GFP if the GFP^{11}-

115   fused protein exists in the same compartment. These results support the conclusion that Atg39

116   specifically localizes to the ONM.

117

118   **APHs of Atg39 bind to the INM to retain Atg39 in the NE**

119   Because the ONM is continuous with the ER membrane, a mechanism must exist that retains

120   Atg39 in the ONM. The determined topology of Atg39 suggests that the C-terminal region (165-

121   398) is exposed to the perinuclear space; however, the importance and function of this region in

122   nucleophagy have yet to be investigated. We therefore examined the intracellular localization of

123   C-terminally truncated Atg39 mutants (Fig. 2A, B). Whereas Atg39$^{1-347}$ and Atg39$^{1-325}$, as with

124   wild-type Atg39, exhibited specific localization to the ONM, Atg39$^{1-296}$ and Atg39$^{1-194}$ leaked out

125   into the ER, which spreads mainly beneath the plasma membrane in yeast cells (West et al., 2011).

126   In contrast, deletion of the N-terminal cytoplasmic region did not affect the ONM localization of

127   Atg39 (Fig. S1A). These results suggest that the C-terminal region 297-325 is responsible for

128   limiting Atg39 localization to the ONM.

129   In analysis of the localization of N-terminally truncated Atg39 mutants, we found that

130   the mutant lacking cytoplasmic and transmembrane domains (Atg39$^{167-398}$) localized to the surface

131   of lipid droplets (Fig. S1A, B). Although this is an artifact of cytoplasmic expression of the

132   perinuclear space region, it raised the possibility that the perinuclear space region of Atg39 has

133   the ability to associate with lipid membranes. The C-terminal region of Atg39 is predicted to

134   largely form a helical conformation, containing at least three APHs, including helix 297-324

135   (APH$^{297-324}$), which is important for the ONM localization of Atg39 (Fig. 2A, B). APHs are known

136   to bind to membranes through their hydrophobic surface (Drin and Antonny, 2010). We therefore

137   speculated that APH$^{297-324}$ associates with the INM from the side of the perinuclear space to

138   prevent Atg39 from leaking into the ER. To examine this possibility, nine hydrophobic residues

139   in APH$^{297-324}$ were replaced with alanine (9A) (Fig. 2C). Similar to Atg39$^{1-296}$, this 9A mutant

140   mislocalized to the ER, highlighting the importance of the amphipathic property of APH$^{297-324}$ in

141   Atg39 retention to the ONM.

142   Next, we performed a co-flotation assay using liposomes and purified APH$^{297-324}$ tagged

143   with GFP-GST (Fig. 2D). Although APH$^{297-324}$-GFP-GST co-floated with small liposomes (~40

144   nm in diameter) after centrifugation, the 9A mutation severely impaired liposome binding of this

145   fusion protein, demonstrating that APH$^{297-324}$ indeed has a membrane-binding ability. To clarify

146   that the APHs of Atg39 associate with the INM in the perinuclear space, we performed

147   immunoelectron microscopy of an Atg39 variant in which the HA sequence was inserted into the

148   region between APH$^{297-324}$ and APH$^{365-379}$ (Fig. S1C). Reaction of the immunogold particles with

149   the HA sequence was frequently detected in the vicinity of the INM. Overall, these findings

150 suggest that, in addition to the transmembrane domain, which penetrates the ONM, Atg39

151 contains membrane-binding APHs and is exclusively localized to the ONM via the insertion of

152 APHs into the perinuclear space-facing layer of the INM (Fig. 2E). These two types of membrane-

153 binding domains bridging the ONM and INM allowed us to speculate that Atg39 couples

154 deformation of the ONM and INM during NDV formation in nucleophagy.

155

156 **APHs of Atg39 promote Atg39 assembly at the NDV formation site**

157 Next, we examined nucleophagy in APH-deleted Atg39 mutants. Nucleophagy activity can be

158 evaluated by the amounts of protease-resistant GFP fragments (GFP') generated by vacuolar

159 degradation of the nucleoplasmic protein Tal1 (Breker et al., 2014) fused with GFP. The results

160 showed that the Atg39$^{1-296}$ and Atg39$^{1-194}$ mutants were severely defective in nucleophagy and that

161 the Atg39$^{1-347}$ mutant had a milder defect (Fig. 3A), confirming that the APHs of Atg39 are

162 important for nucleophagy.

163   Next, we determined which nucleophagy step is defective in Atg39 mutants lacking the

164 APHs. To this end, we first determined the intracellular dynamics of Atg39 during the process of

165 nucleophagy. Because the expression of Atg39 is repressed under normal conditions (Mochida et

166 al., 2015), in these experiments, we expressed Atg39 using the constitutive *HRR25* promoter and

167 observed changes in Atg39 localization upon rapamycin treatment (nucleophagy induction).

168 Before adding rapamycin, Atg39-mCherry was almost uniformly distributed in the NE, although

169 a significant proportion of cells had faint Atg39-mCherry puncta that did not colocalize with the

170 autophagosomal membrane marker Atg8 tagged with mNeonGreen (mNG) (Fig. 3B). In contrast,

171 30 min after rapamycin addition, Atg39-mCherry assembled and formed bright puncta that

172 colocalized with mNG-Atg8, and after 3 h, these puncta disappeared, and mCherry and mNG

173 fluorescence was observed within the vacuole, showing the progression of nucleophagy (Fig. 3B).

174   Moreover, after 30 min of rapamycin treatment, the NE frequently formed protrusions (or buds),

175   with notable accumulation of Atg39-mCherry (Fig. 3B). Colocalization of the INM protein Heh1

176   suggests that the INM protrudes together with the ONM (Fig. 3C). These results further suggest

177   that NE protrusions associated with bright Atg39-mCherry puncta represent forming NDVs. In

178   contrast, the bright puncta of Atg39-mCherry did not form in cells lacking the core Atg protein

179   Atg1 or Atg2, and this was also the case in cells lacking the adapter protein Atg11, which recruits

180   the core Atg proteins (Fig. S2). Meanwhile, the formation of Atg8-negative, faint Atg39-mCherry

181   puncta, which did not increase following rapamycin treatment (Fig. 3B), was largely unaffected

182   by deletion of genes encoding these proteins (Fig. S2). These results suggest that Atg39 partially

183   assembles in the NE, and that this assembly is strongly enhanced in line with the formation of the

184   autophagosomal membrane.

185   As with the membrane-binding APHs analyzed previously (Drin and Antonny, 2010),

186   APH$^{297\text{-}324}$ of Atg39 preferentially bound to smaller liposomes (membranes with high positive

187   curvature) (Fig. 2D). Because protruding membrane domains have higher curvature than other

188   parts of the NE, it is possible that the APHs of Atg39 sense the local curvature in the INM during

189   assembly. Indeed, deletion of the APHs decreased the formation of both faint (rapamycin-

190   independent, Atg8-negative) and bright (rapamycin-dependent, Atg8-positive) Atg39-mCherry

191   puncta (Fig. 3D). These results suggest that the APHs of Atg39 are involved in both basal and

192   enhanced Atg39 assembly in the NE. As mentioned above, enhanced Atg39 assembly depends on

193   autophagosome formation (Fig. S2), and thus it is likely that autophagosome formation in the

194   cytoplasm and APHs bound to the INM act together to assemble Atg39 at the site of NDV

195   formation.

196

197   **APHs of Atg39 are involved in deformation of the NE during NDV formation**

198   The insertion of APHs into one side of the lipid bilayer can bend the membrane (Drin and Antonny,

199   2010). We therefore examined whether Atg39 itself can induce local NE remodeling for the

200   generation of NDVs. Atg39-mCherry was overexpressed using the copper-inducible *CUP1*

201   promoter in *atg1Δ* cells to block nucleophagy and accumulate Atg39-mCherry in the NE. We

202   found that the accumulation of Atg39 in the NE caused the extension of tubules from the NE (Fig.

203   4A), consistent with a previous report (Vevea et al., 2015). Rapamycin treatment increased the

204   formation of these NE tubules in terms of both number and length (Fig. 4A) in *atg1Δ* cells. In

205   addition, deletion of neither *ATG8* nor *ATG11* affected this tubule formation (Fig. S3A),

206   suggesting that rapamycin treatment promotes NE tubule formation independent of

207   autophagosome formation and the interactions of Atg39 with Atg8 and Atg11. Electron

208   microscopy further confirmed that both the ONM and INM join to form these tubules (Fig. 4B).

209   The tips of the tubules were often swollen and contained components similar to the nucleoplasm,

210   consistent with the idea that these structures are related to NDV formation. We also showed that

211   the formation of NE tubules was much less efficient in cells overexpressing Atg39[1-296] compared

212   with the wild-type Atg39, suggesting that the APHs of Atg39 are involved in NE tubulation (Fig.

213   4C). Taken together, these findings suggest that Atg39 has the ability to induce the protrusion of

214   both the ONM and INM to form NDVs, with the perinuclear-space APHs playing an important

215   role. Although NE tubulation is an exaggerated phenomenon caused by Atg39 overexpression,

216   puncta of endogenous Atg39 were often observed at the tip of the NE protrusions (Fig. S3B).

217   Furthermore, time-lapse microscopy showed that budding and fission of Atg39-mCherry-

218   enriched structures occur at the tip of NE tubules (Fig. S3C). Overall, these results suggest that

219   endogenous Atg39 also deforms the NE and generates short protrusions, the tip of which provides

220   a site for NDV formation.

221

222 **Chromosomes are excluded from NE tubules and NDVs**

223 Lastly, we investigated the incorporation of nuclear components into NE tubules under Atg39

224 overexpression. Consistent with the electron microscopic observations showing that these tubules

225 are composed of both the ONM and INM (Fig. 4B), fluorescence microscopy showed signals of

226 the INM protein Heh1 in most of tubules positive for Atg39 (Fig. 5A). Moreover, although less

227 but significant proportions of NE tubules also contained the nucleoplasmic protein Tal1 and the

228 nucleolar protein Nop56, the histone H2A Hta2 seldom colocalized with these tubules. We also

229 confirmed that histone proteins were absent from NDVs formed using cells lacking Ypt7, a Rab

230 GTPase essential for autophagosome-vacuole fusion (Kirisako et al., 1999). When these cells

231 were treated with rapamycin, numerous Atg39-mCherry puncta representing NDVs sequestered

232 within the autophagosomes accumulated in the cytoplasm (Fig. 5B). Whereas puncta of Tal1-GFP

233 were observed outside the nucleus, colocalizing with cytoplasmic Atg39-mCherry puncta, the

234 GFP-fused histones Hta2 and Htz1 did not form any puncta (Fig. 5B). Moreover, Hoechst-stained

235 DNA was not detected in Atg39-mCherry puncta in these cells (Fig. S4), suggesting that

236 chromosomes do not enter NE protrusions and are excluded from sequestration into NDVs.

237

238 **Discussion**

239 In this study, we showed that the nucleophagy receptor Atg39 is a single membrane-spanning

240 ONM protein whose N-terminal cytoplasmic region interacts with Atg8 and Atg11 and whose C-

241 terminal perinuclear space region contains APHs that associate with the INM. Deletion of these

242 APHs resulted in Atg39 mislocalization to the ER, with impaired basal (autophagosome

243 formation-independent) and enhanced (autophagosome formation-dependent) assembly in the NE

244 as well as reduced nucleophagy activity. Overexpression of Atg39 induced the extension of double

245 membrane tubules from the NE depending on the APHs. Based on these results, we propose the

246   following model for the mechanism of NDV formation during Atg39-mediated nucleophagy (Fig.

247   6). First, a certain amount of Atg39 assembles in the NE in a manner dependent on its APHs and

248   independent of autophagosome formation (GFP-Atg8-negative Atg39-mCherry puncta).

249   Dependency of this basal Atg39 assembly on the APHs suggests that at least the INM protrudes

250   into the perinuclear space at this stage. The APHs of Atg39 and/or other proteins (see below) may

251   also be involved in this initial deformation of the NE/INM. The cytoplasmic region of Atg39 in

252   the assemblage subsequently recruits the core Atg proteins via Atg11, thereby initiating

253   autophagosome formation on the NE. Atg39 then assembles further, probably via interaction with

254   Atg11 and the core Atg proteins associated with the isolation membrane such as Atg8, thereby

255   inducing protrusion of the INM into the perinuclear space through the APHs while remaining

256   anchored to the ONM in the transmembrane domain, resulting in the formation of double

257   membrane protrusions out of the NE. Both the ONM and INM cause fission at the tip of the

258   protrusions, resulting in the formation of NDVs containing intranuclear components, which are

259   then sequestered into the autophagosomes and delivered to the vacuole for degradation.

260   Although membrane bending via the wedging effect of APH insertion has been well

261   documented, the findings suggest that the perinuclear space region of Atg39 also generates

262   membrane curvature through an additional mechanism that can cooperate with the wedging

263   mechanism. For example, a number of BAR proteins contain APHs and form crescent-shaped

264   dimers, which serve as scaffolds and act together with the APHs to tubulate membranes

265   (Baumgart et al., 2011). Steric pressure generated by local crowding of peripheral membrane

266   proteins can also cause the tubulation of flat membranes (Stachowiak et al., 2012). Structural and

267   in vitro studies of the perinuclear space region of Atg39 should further clarify the detailed

268   mechanisms by which this region drives NE deformation. In addition, it is also possible that Atg39

269   in the cytoplasm and perinuclear space recruits other membrane-deforming proteins to generate

270   NDVs. It should be noted that tubules extending without the INM were also observed in Atg39-

271   overexpressing cells (Fig. 5A, S3D). These ONM tubules were not formed when Atg39 lacking

272   the APHs was overexpressed. This observation may be merely an artifact of Atg39 overexpression

273   but imply that the APHs of Atg39 are also involved in ONM deformation. However, because the

274   perinuclear space surface of the protruding ONM has negative curvature, the perinuclear space

275   region other than the APHs might contribute to deformation of the ONM.

276   Although the mechanism of NDV fission from the NE remains unknown, the ESCRT-

277   III complex is a potential candidate for fission of the INM. ESCRT-III proteins form spiral

278   filaments and mediate the invagination and fission of intralumenal vesicles in late endosomes,

279   and these proteins are also known to exist on the nucleoplasmic surface of the INM, where they

280   cause NE deformation similar to that observed in nucleophagy (McCullough et al., 2018; Lee et

281   al., 2012; Webster et al., 2014). During the nucleus-to-cytoplasm exit of some herpesviruses, the

282   INM, in association with nucleocapsids, invaginates and causes fission depending on ESCRT-III

283   to release nucleocapsid-containing vesicles into the perinuclear space (Arii et al., 2018; Lee et al.,

284   2012). Similarly, ESCRT-III may contribute to initial deformation, protrusion, and fission of the

285   INM during NDV formation in nucleophagy. The molecular mechanism of ONM fission also

286   remains unclear, but is thought to involve membrane-deforming proteins such as dynamin-related

287   proteins and reticulon-family proteins, which are reported to mediate organelle fission during

288   selective autophagy of mitochondria and the ER, respectively (Mao et al., 2013; Khaminets et al.,

289   2015; Mochida et al., 2020).

290   In this study, INM insertion of the APHs was found to be important for the NE retention

291   of Atg39. However, continuity between the ONM and the ER membrane poses the further

292   question of why the APHs of Atg39 associate with the INM in the NE, but not with the opposite

293   membrane in the ER. The difference in thickness (the distance between the two opposing

294   membranes) might be one answer to this question, given that the ER is thicker than the NE in *S.*

295   *cerevisiae* (West et al., 2011), which might prevent the APHs of Atg39 from reaching the opposite

296   membrane in the ER. Atg39 that has been synthesized in the ER is diffused to the NE and anchored

297   to the INM via the APHs or degraded in the ER due to unstable APHs without membrane insertion.

298   It is also conceivable that Atg39 APHs disfavor the lumen-facing leaflet of the ER due to its

299   flatness or negative curvature, especially with the tubular ER. The perinuclear space region of

300   Atg39 may also contain a sequence interacting with an INM protein, which cooperates with the

301   APHs in Atg39 anchoring to the INM.

302   Although nucleophagy is thought to be advantageous for cells in that it can serve as a

303   powerful system for quality and quantity control of nuclear components, it must avoid degrading

304   components such as chromosomes that are essential for cell viability. In this study, we showed

305   that NE protrusions induced by overexpression of Atg39, as well as NDVs, do not contain histones

306   and DNA. We speculate that NE protrusions are thin enough to block the entry of chromosomes

307   into NDVs, guaranteeing the safety in degradation of the nucleus.

308   NDV formation during nucleophagy is associated with complicated membrane dynamics

309   in the NE. This study focused on the APHs of Atg39, providing a deeper understanding of the

310   underlying mechanism. However, unresolved issues remain, including how NE deformation and

311   autophagosome formation cooperate as well as how membrane fission occurs to release NDVs

312   from NE protrusions. Further analysis of Atg39 and identification of other proteins involved in

313   nucleophagy will be important in addressing these issues.

314

315 **Materials and methods**

316 **Yeast strains and plasmids**

317 Yeast strains used in this study are listed in Table S1. Gene deletion and tagging were based on a

318 standard PCR-based method (Janke et al., 2004). pRS303-derived plasmids were integrated into

319 the genome at the *HIS3* locus after linearization using the restriction enzyme *Nsi*I (Sikorski and

320 Hieter, 1989; Janke et al., 2004). Plasmids used in this study are listed in Table S2. They were

321 constructed by amplifying appropriate DNA fragments by PCR and assembling them using the

322 Gibson Assembly method (New England Biolabs). pRS315-NOP1pro-GFP$^{1\text{-}10}$-mCherry-PUS1

323 and pRS315-NOP1pro-GFP$^{1\text{-}10}$-mCherry-SCS2TM were generated using PCR products amplified

324 from Addgene plasmids #86413 and #86419 and Addgene plasmids #86416 and #86419,

325 respectively.

326

327 **Yeast cell growth conditions**

328 Yeast cells were grown at 30°C in YPD medium (1% yeast extract, 2% peptone, and 2% glucose)

329 or SD+CA medium (0.17% yeast nitrogen base without amino acids and ammonium sulphate,

330 0.5% ammonium sulfate, 0.5% casamino acids, and 2% glucose) appropriately supplemented with

331 0.002% adenine, 0.002% uracil, and 0.002% tryptophan. For nucleophagy induction, cells were

332 grown to mid-log phase and treated with 200 ng/mL rapamycin. For Atg39 overexpression, cells

333 in which *ATG39* was put under the control of the *CUP1* promoter were grown in SD+CA medium

334 containing 250 μM CuSO$_4$ overnight. In Fig. 3D, cells expressing mCherry-tagged wild-type

335 Atg39 were grown in SD+CA medium containing 10 μM CuSO$_4$ overnight. To develop large lipid

336 droplets (Fig. S1B), cells were grown in SO+CA medium (0.17% yeast nitrogen base without

337 amino acids and ammonium sulphate, 0.5% ammonium sulfate, 0.12% oleate, 0.2% Tween 40,

338 0.1% glucose, 1% casamino acids, 0.1% yeast extract, 0.002% adenine sulfate, 0.002%

339   tryptophan, and 0.002% uracil) for 9 h.

340

341   **Cell lysate extraction and immunoblotting**

342   Frozen yeast cells were resuspended in 200 mM NaOH and left on ice for 5 min. After

343   centrifugation at 3,000 g and removal of the supernatants, the cell pellets were resuspended in

344   urea SDS sample buffer [100 mM MOPS-KOH (pH 6.8), 4% SDS, 100 mM dithiothreitol (DTT),

345   and 8 M urea] and incubated at 65°C for 10 min. Proteins were resolved by SDS-PAGE,

346   transferred to PVDF membranes, and incubated with primary antibodies against GFP (Clontech,

347   632381), HA (Roche, 11867431001), mRFP (a gift from Dr. Toshiya Endo), and Kar2 (a gift from

348   Dr. Toshiya Endo). After incubation with HRP-conjugated secondary antibodies, the blots were

349   visualized using ImageQuant LAS 4000 (GE Healthcare).

350

351   **Fluorescence microscopy**

352   Yeast cells were analyzed using two different fluorescence microscopy systems, as described

353   previously (Mochida et al., 2020). The images in Fig. 1D, 5B, S1A, S3C, and S4 were acquired

354   using an inverted microscope (IX81; Olympus) equipped with an electron-multiplying CCD

355   camera (ImagEM C9100-13; Hamamatsu Photonics), a 150× objective lens (UAPON

356   150XOTIRF, NA/1.45; Olympus), a Z drift compensator (IX3-ZDC2; Olympus), and appropriate

357   lasers and filters. For time-lapse imaging, cells were grown in the glass-bottom dish and kept at

358   30°C using a stage top incubator (TOKAI HIT). The images in Fig. S3C were deconvoluted by

359   AutoQuant X3 software (Media Cybernetics). All other fluorescence microscopy images were

360   acquired using a Delta Vision Elite microscope system (GE Healthcare) equipped with a scientific

361   CMOS camera (pco.edge 5.5; PCO AG) and a 60× objective lens (PLAPON, NA/1.42; Olympus).

362   Images acquired by a Delta Vision were deconvoluted using SoftWoRx software. All acquired

363   images were analyzed using Fiji software (Schindelin et al., 2012).

364

365   **Quantification of fluorescence microscopy images**

366   Atg39-mCherry puncta and mNG-Atg8 puncta were detected using the Find Maxima function of

367   Fiji as described previously (Mochida et al., 2020). When the maxima of Atg39-mCherry puncta

368   exists within 272 nm of those of GFP- or mNG-Atg8 puncta, they were classified as GFP/mNG-

369   Atg8-positive. The number of the Atg39-mCherry-positive tubules extending from the NE was

370   manually counted. The length of the NE tubules was measured using the segmented line selection

371   tool of Fiji. In branched tubules, the length of the longest tubule was measured.

372

373   **Proteinase K protection assay**

374   Yeast cells grown to mid-log phase were washed with 100 mM Tris-HCl (pH 8.0) containing 10

375   mM DTT and then converted to spheroplasts by incubation in 0.5×YPD containing 1 M sorbitol

376   and 200 µg/mL zymolyase 100T (Nacalai Tesque) at 30°C for 30 min. Cells were washed with 20

377   mM HEPES-KOH (pH 7.2) containing 1.2M sorbitol and incubated in 0.5×YPD containing 1 M

378   sorbitol and 200 ng/mL rapamycin for 3 h. After centrifugation, pelleted cells were resuspended

379   in HSE buffer (20 mM HEPES-KOH (pH 7.2), 1M sorbitol, and 1mM EDTA) containing 0.5 ×

380   Complete protease inhibitor cocktail (PIC) (Roche) and were passed through a polycarbonate

381   membrane filter with a 3-µm pore size (Merck Millipore). The supernatants (lysates) were

382   obtained by removing cell debris by centrifugation then treated with 1% Triton X-100 and 100

383   µg/mL proteinase K on ice for 30 min. Proteolysis was stopped by the addition of 10 mM

384   phenylmethylsulfonyl fluoride (PMSF), and after trichloroacetic acid precipitation, the proteins

385   were solubilized in urea SDS sample buffer and analyzed by immunoblotting.

386

387 **Protein purification**

388 BJ3505 cells overexpressing Atg39$^{297\text{-}324}$-GFP-GST, Atg39$^{297\text{-}324\ 9A}$-GFP-GST, or GFP-GST were

389 grown to late-log phase and harvested. Frozen cells were resuspended in buffer A [50 mM Tris-

390 HCl (pH 7.5), 500 mM NaCl, 1 mM EDTA, and 10% glycerol] containing 2 × PIC, 2 mM PMSF,

391 and 1 mM DTT, disrupted using a Multi-beads Shocker (Yasui Kikai) and 0.5-mm YZB zirconia

392 beads, and solubilized with 1% Triton X-100. The lysates were cleared by centrifugation at

393 100,000 g at 4°C for 30 min and then mixed with Glutathione Sepharose 4B (GE Healthcare).

394 The Sepharose beads were washed with buffer B [50 mM Tris-HCl (pH 8.0), 500 mM NaCl, 1

395 mM EDTA, and 10% glycerol] containing 0.01% Triton X-100, and then the bound proteins were

396 eluted with buffer B containing 0.01% Triton X-100 and 10 mM reduced glutathione.

397

398 **Liposome flotation assay**

399 Liposomes were prepared as follows. Lipids in chloroform were mixed (55:25:20:0.005 mole

400 percent POPC:DOPE:bovine liver PI:Rhodamine-DOPE) and dried in a glass tube. The lipid film

401 was hydrated with buffer C [20 mM HEPES-KOH (pH 7.2) and 150 mM NaCl] at a lipid

402 concentration of 1 mM before the suspension was repeatedly frozen and thawed. To prepare larger

403 liposomes, the liposome suspension was extruded through a polycarbonate membrane filter with

404 a 200-nm pore size (Merck Millipore). Smaller liposomes were prepared by sonicating the

405 liposome suspension. The size of the liposomes was measured using a Zetasizer Nano S (Malvern

406 Instruments).

407   40 µL of the prepared liposomes was mixed with 5 µL of 250 nM protein solution and

408 80 µL of buffer C, and incubated for 1 h at 30°C. 125 µl of 100% OptiPrep (Abbott Diagnostics

409 Technologies AS) was added to the mixture, which was then overlaid with 450 µL of buffer C

410 containing 40% OptiPrep and 200 µL of Optiprep-free buffer C. After centrifugation at 200,000

411   *g* at 4°C for 105 min, the top, middle, and bottom fractions (300 μL each) were collected, and

412   GFP fluorescence in each fraction was measured using a Varioskan Flash (Thermo Scientific).

413

414   **Electron microscopy**

415   Electron microscopy was performed by Tokai-EMA Inc. Yeast cells were sandwiched with copper

416   disks, rapidly frozen at −175°C, and freeze-substituted with ethanol containing 2% glutaraldehyde

417   and 0.5% tannic acid. After dehydration, the samples were embedded in Quetol-651 resin and

418   ultra-thin sectioned for observation under a transmission electron microscopy (JEM-1400Plus;

419   JEOL). For immunoelectron microscopy, the samples were prepared in a similar manner, except

420   that cells were freeze-substituted with ethanol containing 1% tannic acid and 2% water and

421   embedded in LR white resin. The sections were incubated with an antibody against HA

422   (11867431001, Roche) and then with a secondary antibody-conjugated to 10-nm gold particles.

423

424   **Acknowledgements**

435   discussed the results and commented on the manuscript.

436

437   **References**

438   Arii, J., M. Watanabe, F. Maeda, N. Tokai-Nishizumi, T. Chihara, M. Miura, Y. Maruzuru, N.

439   Koyanagi, A. Kato, and Y. Kawaguchi. 2018. ESCRT-III mediates budding across the

440   inner nuclear membrane and regulates its integrity. *Nat. Commun.* 9. doi:10.1038/s41467-

441   018-05889-9.

442   Baumgart, T., B.R. Capraro, C. Zhu, and S.L. Das. 2011. Thermodynamics and mechanics of

443   membrane curvature generation and sensing by proteins and lipids. *Annu. Rev. Phys.*

444   *Chem.* 62:483–506. doi:10.1146/annurev.physchem.012809.103450.

445   Breker, M., M. Gymrek, O. Moldavski, and M. Schuldiner. 2014. LoQAtE—Localization and

446   Quantitation ATlas of the yeast proteomE. A new tool for multiparametric dissection of

447   single-protein behavior in response to biological perturbations in yeast. *Nucleic Acids Res.*

448   42:D726–D730. doi:10.1093/nar/gkt933.

449   Dou, Z., C. Xu, G. Donahue, T. Shimi, J.-A. Pan, J. Zhu, A. Ivanov, B.C. Capell, A.M. Drake,

450   P.P. Shah, J.M. Catanzaro, M. Daniel Ricketts, T. Lamark, S.A. Adam, R. Marmorstein,

451   W.-X. Zong, T. Johansen, R.D. Goldman, P.D. Adams, and S.L. Berger. 2015. Autophagy

452   mediates degradation of nuclear lamina. *Nature.* 527:105–109. doi:10.1038/nature15548.

453   Drin, G., and B. Antonny. 2010. Amphipathic helices and membrane curvature. *FEBS Lett.*

454   584:1840–1847. doi:10.1016/j.febslet.2009.10.022.

455   Enam, C., Y. Geffen, T. Ravid, and R.G. Gardner. 2018. Protein Quality Control Degradation in

456   the Nucleus. *Annu. Rev. Biochem.* 87:725–749. doi:10.1146/annurev-biochem-062917-

457   012730.

458   Farré, J.-C., and S. Subramani. 2016. Mechanistic insights into selective autophagy pathways:

459   lessons from yeast. *Nat. Rev. Mol. Cell Biol.* 17:537–52. doi:10.1038/nrm.2016.74.

460   Janke, C., M.M. Magiera, N. Rathfelder, C. Taxis, S. Reber, H. Maekawa, A. Moreno-Borchart,

461   G. Doenges, E. Schwob, E. Schiebel, and M. Knop. 2004. A versatile toolbox for PCR-

462   based tagging of yeast genes: New fluorescent proteins, more markers and promoter

463   substitution cassettes. *Yeast*. doi:10.1002/yea.1142.

464   Khaminets, A., T. Heinrich, M. Mari, P. Grumati, A.K. Huebner, M. Akutsu, L. Liebmann, A.

465   Stolz, S. Nietzsche, N. Koch, M. Mauthe, I. Katona, B. Qualmann, J. Weis, F. Reggiori, I.

466   Kurth, C.A. Hübner, and I. Dikic. 2015. Regulation of endoplasmic reticulum turnover by

467   selective autophagy. *Nature*. 522:354–358. doi:10.1038/nature14498.

468   Kirisako, T., M. Baba, N. Ishihara, K. Miyazawa, M. Ohsumi, T. Yoshimori, T. Noda, and Y.

469   Ohsumi. 1999. Formation Process of Autophagosome Is Traced with Apg8 / Aut7p in

470   Yeast. *Jcb*. 147:435–446. doi:10.1083/jcb.147.2.435.

471   Lee, C.P., P.T. Liu, H.N. Kung, M.T. Su, H.H. Chua, Y.H. Chang, C.W. Chang, C.H. Tsai, F.T.

472   Liu, and M.R. Chen. 2012. The ESCRT Machinery Is Recruited by the Viral BFRF1

473   Protein to the Nucleus-Associated Membrane for the Maturation of Epstein-Barr Virus.

474   *PLoS Pathog.* 8. doi:10.1371/journal.ppat.1002904.

475   Lee, C.W., F. Wilfling, P. Ronchi, M. Allegretti, S. Mosalaganti, S. Jentsch, M. Beck, and B.

476   Pfander. 2020. Selective autophagy degrades nuclear pore complexes. *Nat. Cell Biol.*

477   doi:10.1038/s41556-019-0459-2.

478   Mao, K., K. Wang, X. Liu, and D.J. Klionsky. 2013. The scaffold protein Atg11 recruits fission

479   machinery to drive selective mitochondria degradation by autophagy. *Dev. Cell*. 26:9–18.

480   doi:10.1016/j.devcel.2013.05.024.

481   McCullough, J., A. Frost, and W.I. Sundquist. 2018. Structures, Functions, and Dynamics of

482   ESCRT-III/Vps4 Membrane Remodeling and Fission Complexes. *Annu. Rev. Cell Dev.*

483   *Biol.* 34:85–109. doi:10.1146/annurev-cellbio-100616-060600.

484   Mijaljica, D., and R.J. Devenish. 2013. Nucleophagy at a glance. *J. Cell Sci.* 126:4325–4330.

485   doi:10.1242/jcs.133090.

486   Mochida, K., Y. Oikawa, Y. Kimura, H. Kirisako, H. Hirano, Y. Ohsumi, and H. Nakatogawa.

487   2015. Receptor-mediated selective autophagy degrades the endoplasmic reticulum and the

488   nucleus. *Nature*. 522:359–362. doi:10.1038/nature14506.

489   Mochida, K., A. Yamasaki, K. Matoba, H. Kirisako, N.N. Noda, and H. Nakatogawa. 2020.

490   Super-assembly of ER-phagy receptor Atg40 induces local ER remodeling at contacts with

491   forming autophagosomal membranes. *Nat. Commun.* 11. doi:10.1038/s41467-020-17163-

492   y.

493   Morishita, H., and N. Mizushima. 2019. Diverse Cellular Roles of Autophagy. *Annu. Rev. Cell*

494   *Dev. Biol.* 35:453–475. doi:10.1146/annurev-cellbio-100818-125300.

495   Nakatogawa, H. 2020. Mechanisms governing autophagosome biogenesis. *Nat. Rev. Mol. Cell*

496   *Biol.* doi:10.1038/s41580-020-0241-0.

497   Schindelin, J., I. Arganda-Carreras, E. Frise, V. Kaynig, M. Longair, T. Pietzsch, S. Preibisch,

498   C. Rueden, S. Saalfeld, B. Schmid, J.Y. Tinevez, D.J. White, V. Hartenstein, K. Eliceiri, P.

499   Tomancak, and A. Cardona. 2012. Fiji: An open-source platform for biological-image

500   analysis. *Nat. Methods*. 9:676–682. doi:10.1038/nmeth.2019.

501   Sikorski, R.S., and P. Hieter. 1989. A system of shuttle vectors and yeast host strains designed

502   for efficient manipulation of DNA in Saccharomyces cerevisiae. *Genetics*.

503   doi:0378111995000377 [pii].

504   Smoyer, C.J., S.S. Katta, J.M. Gardner, L. Stoltz, S. McCroskey, W.D. Bradford, M. McClain,

505   S.E. Smith, B.D. Slaughter, J.R. Unruh, and S.L. Jaspersen. 2016. Analysis of membrane

506   proteins localizing to the inner nuclear envelope in living cells. *J. Cell Biol.* 215:575–590.

507   doi:10.1083/jcb.201607043.

508   Stachowiak, J.C., E.M. Schmid, C.J. Ryan, H.S. Ann, D.Y. Sasaki, M.B. Sherman, P.L.

509   Geissler, D.A. Fletcher, and C.C. Hayden. 2012. Membrane bending by protein-protein

510   crowding. *Nat. Cell Biol.* 14:944–9. doi:10.1038/ncb2561.

511   Tomioka, Y., T. Kotani, H. Kirisako, Y. Oikawa, Y. Kimura, H. Hirano, Y. Ohsumi, and H.

512   Nakatogawa. 2020. TORC1 inactivation stimulates autophagy of nucleoporin and nuclear

513   pore complexes. *J. Cell Biol.* 219. doi:10.1083/jcb.201910063.

514   Vevea, J.D., E.J. Garcia, R.B. Chan, G. Di Paolo, J.M. Mccaffery, L.A. Pon, J.D. Vevea, E.J.

515   Garcia, R.B. Chan, B. Zhou, M. Schultz, G. Di Paolo, J.M. Mccaffery, and L.A. Pon.

516   2015. Role for Lipid Droplet Biogenesis and Microlipophagy in Adaptation to Lipid

517   Imbalance in Article Role for Lipid Droplet Biogenesis and Microlipophagy in Adaptation

518   to Lipid Imbalance in Yeast. *Dev. Cell*. 35:584–599. doi:10.1016/j.devcel.2015.11.010.

519   Webster, B.M., P. Colombi, J. Jäger, and C. Patrick Lusk. 2014. Surveillance of nuclear pore

520   complex assembly by ESCRT-III/Vps4. *Cell*. doi:10.1016/j.cell.2014.09.012.

521   West, M., N. Zurek, A. Hoenger, and G.K. Voeltz. 2011. A 3D analysis of yeast ER structure

522   reveals how ER domains are organized by membrane curvature. *J. Cell Biol.* 193:333–346.

523   doi:10.1083/jcb.201011039.

524   Woulfe, J. 2008. Nuclear bodies in neurodegenerative disease. *Biochim. Biophys. Acta*.

525   1783:2195–206. doi:10.1016/j.bbamcr.2008.05.005.

526

527

528 **Figure Legends**

529 **Figure 1. Atg39 is a transmembrane protein embedded in the ONM.**

530 **(A, B)** Proteinase K protection assay was performed to determine the membrane topology of

531 Atg39. Lysates were prepared from cells expressing HA-Atg39-GFP (A) or Atg39-GFP (B) and

532 incubated with proteinase K (Prot. K) in the absence or presence of Triton X-100 (TX-100). N-

533 terminal HA and C-terminal GFP tags were detected by immunoblotting using anti-HA and anti-

534 GFP antibodies, respectively. Kar2, an ER lumenal protein.

535 **(C)** Schematic diagram of Atg39. TM, transmembrane domain.

536 **(D)** Split GFP-based assay was carried out to determine the localization of Atg39. An N-terminal

537 fragment of GFP (GFP$^{1\text{-}10}$) and mCherry were fused to a transmembrane domain of Scs2 (GFP$^{1\text{-}}$

538 ^{10}-mCherry-Scs2) or Pus1 (GFP$^{1\text{-}10}$-mCherry- Pus1), and the remaining C-terminal fragment of

539 GFP (GFP^{11}) was fused to the N-terminus of Atg39 or the C-terminus of the INM protein Heh1.

540 Cells expressing these proteins were observed under a fluorescence microscope. Scale bars, 5 μm.

541

542 **Figure 2. The APHs of Atg39 bind to the INM to retain Atg39 at the ONM.**

543 **(A)** Schematic diagram of the C-terminal perinuclear space region of Atg39. Helical wheels were

544 generated using a HeliQuest server.

545 **(B)** mCherry-fused wild-type Atg39 (WT) and C-terminally truncated mutants were expressed

546 under the constitutive *HRR25* promoter and analyzed by fluorescence microscopy. Tal1, a

547 nucleoplasmic protein.

548 **(C)** The localization of Atg39$^{1\text{-}325}$-mCherry and Atg39$^{1\text{-}325\ 9A}$-mCherry was analyzed by

549 fluorescence microscopy.

550 **(D)** Liposome flotation assay was carried out to examine the membrane-binding ability of APH$^{297\text{-}}$

551 ^{325}. Purified GFP-GST-fused proteins were mixed with small (~40 nm) or large (~160 nm)

552 liposomes, and then the liposomes and liposome-bound proteins were floated by

553 ultracentrifugation. Data are shown as means ± s.d. (n = 3).

554 **(E)** The determined membrane topology of Atg39.

555 Scale bars, 5 μm.

556

557 **Figure 3. The APHs of Atg39 promote Atg39 assembly at the site of NDV formation.**

558 **(A)** Nucleophagy activity in *atg39Δ* cells expressing wild-type (WT) Atg39 tagged with the HA

559 sequence or C-terminally truncated mutants. Cells were treated with rapamycin to induce

560 nucleophagy, and degradation of Tal1-GFP was examined by immunoblotting using an anti-GFP

561 antibody. The quantification results are shown as means ± s.d. (n = 3). ****$P < 0.0001$; **$P <$

562 0.01 (Student's *t*-test).

563 **(B)** Cells constitutively expressing Atg39-mCherry were treated with rapamycin and observed

564 under a fluorescence microscope. The number of mNG-Atg8-positive and negative puncta of

565 Atg39-mCherry (bottom left), and the fluorescence intensity of these puncta (bottom right) were

566 measured and are shown graphically. Bars represent means ± s.d. (n = 3) (bottom left). ***$P <$

567 0.001 (Student's *t*-test) (bottom left). ****$P < 0.001$ (Mann–Whitney *U* test) (bottom right).

568 **(C, D)** Cells constitutively expressing Atg39-mCherry were treated with rapamycin for 0.5 h and

569 analyzed by fluorescence microscopy. Fluorescence intensity along the dashed line in (C) was

570 measured and is graphically shown. The bars represent means ± s.d. (n = 3). *$P < 0.05$; **$P <$

571 0.01; ***$P < 0.001$ (Student's *t*-test).

572 Arrow heads, mNG/GFP-Atg8-positive Atg39-mCherry puncta. Arrows, mNG/GFP-Atg8-

573 negative Atg39 puncta.

574 Scale bars, 5 μm (B, D), 2 μm (C).

575

576 **Figure 4. Atg39 accumulation in the NE causes NE tubulation dependent on the APHs.**

577 **(A)** *atg1Δ* cells expressing Atg39-mCherry under the *CUP1* promoter were grown in the presence

578 or absence of 250 μM CuSO$_4$ overnight and treated with rapamycin for 2 h. The percentage of

579 cells containing NE tubules (left) and length of NE tubules (right) are shown. Bars represent

580 means ± s.d. (n =3). *$P < 0.05$; ****$P < 0.0001$ (Tukey's multiple comparisons test) (left). ****P

581 < 0.0001 (Mann–Whitney U test) (right).

582 **(B)** *atg1Δ* cells overexpressing Atg39-mCherry in the presence of copper ions were treated with

583 rapamycin for 2 h, and the nuclear morphology of these cells was examined by electron

584 microscopy. LD, lipid droplet.

585 **(C)** mCherry-fused Atg39 and Atg39$^{1\text{-}296}$ were overexpressed in *atg1Δ* cells. These cells were

586 treated with rapamycin for 2 h, and the formation of NE tubules was analyzed by fluorescence

587 microscopy. Arrowheads, NE tubules. ****$P < 0.0001$ (Tukey's multiple comparisons test).

588 Scale bars, 5 μm (A, C), 200 nm (B).

589

590 **Figure 5. NE tubules and NDVs exclude chromosomes.**

591 **(A)** NE tubule formation was induced by overexpression of Atg39-mCherry in *atg1Δ* cells

592 followed by treatment with rapamycin treatment for 2 h. The colocalization of Atg39-mCherry-

593 positive NE tubules with GFP-fused Heh1, Tal1, Nop56, and Hta2 was examined by fluorescence

594 microscopy. Arrowheads, NE tubules containing GFP signals. The percentage of NE tubules

595 containing nuclear components is shown in the graph. Bars represent means ± s.d. (n =3).

596 **(B)** *ypt7Δ* cells overexpressing Atg39-mCherry were treated with rapamycin for 4 h. Arrowheads,

597 puncta of Tal1-GFP that colocalized with those of Atg39-mCherry. Fluorescence intensity along

598 the dashed line was measured, and the results are shown in the graph.

599 Scale bars, 5 μm

600

601 **Figure 6. Model mechanism of NDV formation in Atg39-mediated nucleophagy.**

602 Atg39 forms a small cluster depending on APHs in the NE region where the INM partially

603 protrudes via an unknown mechanism. Then, Atg39 in the cluster recruits the core Atg proteins

604 via Atg11 on the cytoplasmic surface of the NE, initiating autophagosome formation, which

605 triggers the further assembly of Atg39, probably via interaction with Atg11 and Atg8 on the

606 forming autophagosomal membrane. The condensation of Atg39 locally enhances its APH-

607 dependent membrane-deforming activity, protruding the NE toward the cytoplasm at the site. An

608 unknown mechanism mediates fission of the tip of the protrusion to release a NDV, which is

609 sequestered into the autophagosome via the interaction between Atg39 and Atg8, a canonical

610 function of autophagy receptors.

611

612 **Supplemental Figure Legends**

613 **Figure S1. The perinuclear space region of Atg39 associates with the INM.**

614 **(A)** The intracellular localization of mCherry-fused wild-type Atg39 (WT) and the N-terminally-

615 truncated mutants expressed under the *HRR25* promoter was analyzed by fluorescence

616 microscopy.

617 **(B)** Cells coexpressing Atg39$^{167-398}$-GFP and the lipid droplet protein Osw5 labeled with mCherry

618 were incubated in oleate-containing medium for 9 h to induce large lipid droplet formation and

619 analyzed under a fluorescence microscope.

620 **(C)** The 4×HA sequence was inserted between the APH$^{297-324}$ and APH$^{365-379}$ of Atg39, and cells

621 expressing this Atg39 variant were analyzed by immunoelectron microscopy using anti-HA

622 antibody. Immunogold signals in the vicinity of the INM and ONM were counted and the results

623 are shown in the graph.

624 Scale bars, 5 μm (A, B), 200 nm (C).

625

626 **Figure S2. Atg39 assembly in different *atg* mutants.**

627 Cells constitutively expressing Atg39-mCherry under the *HRR25* promoter were treated with

628 rapamycin for 0.5 h and analyzed by fluorescence microscopy. The number of Atg39-mCherry

629 puncta per cell (top right) and the fluorescence intensity of Atg39-mCherry puncta (including both

630 mNG-Atg8-positive and -negative puncta) (bottom right) are shown. Arrow heads, mNG-Atg8-

631 positive Atg39 puncta. Arrows, mNG-Atg8-negative Atg39 puncta. Bars represent means ± s.d.

632 (n = 3). ***$P < 0.001$ (Student's *t*-test) (top right). ****$P < 0.001$ (Mann–Whitney *U* test) (bottom

633 right). Scale bars, 5 μm

634

635 **Figure S3. Analysis of NE tubules induced by Atg39 overexpression.**

636   **(A)** NE tubule formation was induced by Atg39 overexpression and 2 h rapamycin treatment in

637   *atg1Δ* cells, and the effects of additional deletion of *ATG8* or *ATG11* on tubule formation was

638   examined by fluorescence microscopy. The percentage of cells containing NE tubules (top right)

639   and the length of NE tubules (bottom right) are shown. Bars represent means ± s.d. (n = 3).

640   Statistical significance was determined using Tukey's multiple comparisons test (top right) and

641   the Kruskal-Wallis test (bottom right), respectively. Arrowheads, NE tubules with GFP signals.

642   **(B)** Cells expressing Atg39-mCherry under the own promoter at the original chromosomal locus

643   were treated with rapamycin for 4 h, and Atg39-mCherry puncta formed at the NE protrusion tip

644   were analyzed by fluorescence microscopy. Fluorescence intensity along the dashed line was

645   measured and is shown graphically. Arrowhead, NE protrusion.

646   **(C)** Cells expressing Atg39-mCherry under the *CUP1* promoter were treated with rapamycin for

647   20 min and then fluorescence images were taken at 15-s intervals. Arrowheads, GFP-Atg8-

648   positive Atg39-mCherry puncta at the tip of NE tubules. Arrow, NDV.

649   **(D)** A representative EM image of a NE tubule without the INM (arrowhead) generated in *atg1Δ*

650   cells overexpressing Atg39 and treated with rapamycin treatment for 2 h.

651   Scale bars, 5 µm (A, B), 2 µm (C), 200 nm (D)

652

653   **Figure S4. NDVs do not contain DNA.**

654   *ypt7Δ* cells overexpressing Atg39-mCherry were treated with rapamycin for 8 h, and the DNA

655   was stained with Hoechst 33258. Arrowheads, nuclei. Small puncta marked by asterisks and that

656   did not colocalize with Atg39-mCherry puncta represent mitochondrial DNA. Fluorescence

657   intensity along the dashed line was measured and is shown in the graph. Scale bars, 5 µm.

658

Table S1. Yeast strains used in this study

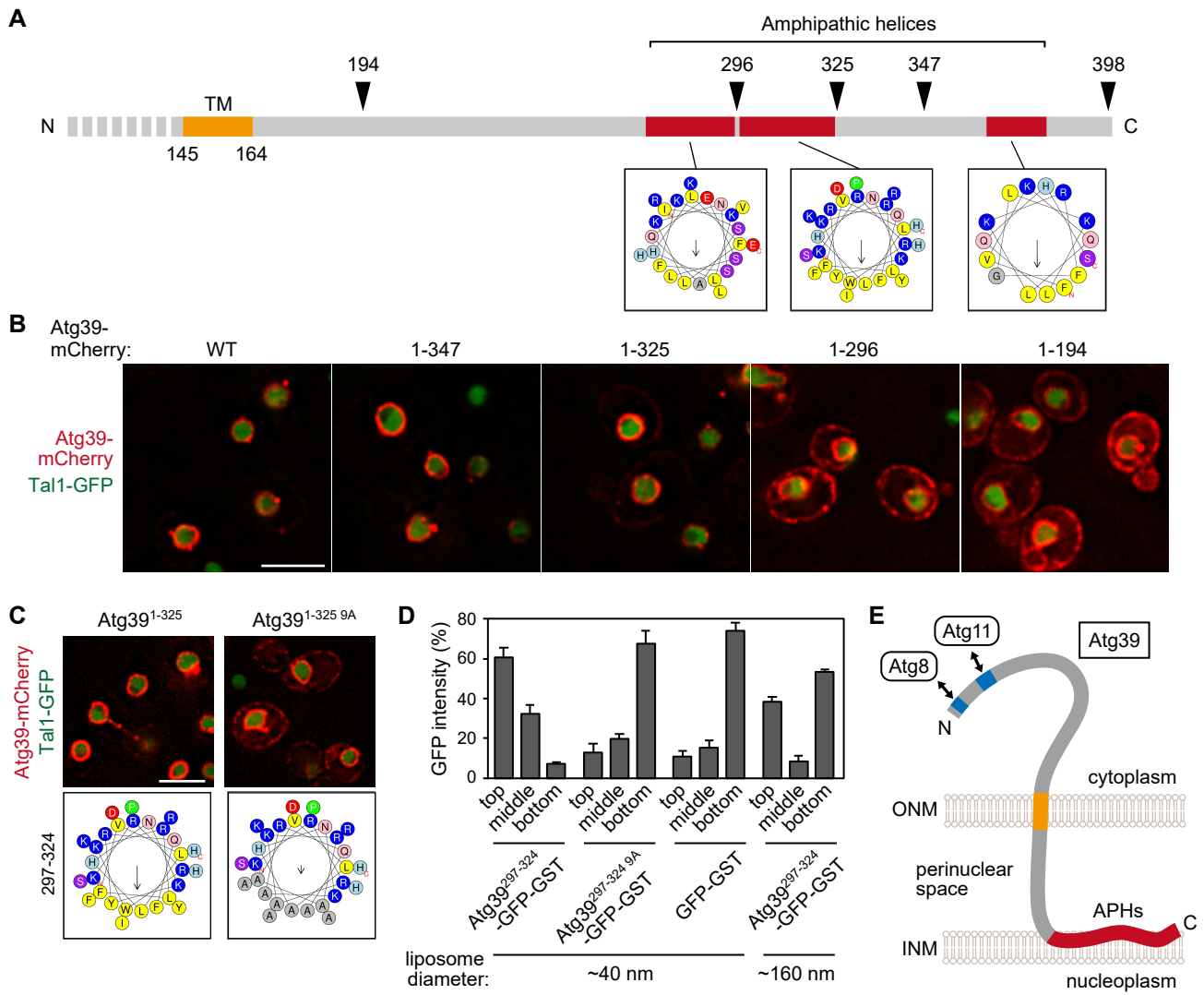| Name	Genotype
YKM976	BJ3505 *natNT2-ADHpro-3HA-ATG39-EGFP-hphNT1 atg1Δ::zeoNT3*
YKM977	BJ3505 *natNT2-ADHpro-ATG39-EGFP-hphNT1 atg1Δ::zeoNT3*
YKM1932	BY4741 *natNT2-HRR25pro-GFP^{11}-ATG39*
YKM1932	BY4741 *natNT2-HRR25pro-GFP^{11}-ATG39*
YKM1938	BY4741 *HEH1-GFP^{11}-natNT2*
YKM1536	BY4741 *TAL1-EGFP-kanMX6 atg39Δ::natNT2*
YKM1998	BY4741 *natNT2-HRR25pro-ATG39-mCherry-hphNT1 his3::mNeonGreen-ATG8-kanMX4*
YKM1094	BY4741 *natNT2-CUP1pro-ATG39-mCherry-hphNT1 his3::GFP-ATG8^{G116}-zeoNT3*
YKY156	BY4741 *natNT2-CUP1pro-ATG39$^{1-296}$-mCherry-kanMX6 his3::GFP-ATG8^{G116}-zeoNT3*
YKM1329	BY4741 *natNT2-CUP1pro-ATG39-mCherry-hphNT1 HEH1-EGFP-kanMX4 atg1Δ::zeoNT3*
YOT61	BY4741 *atg39Δ::natNT2 atg1Δ::zeoNT3 his3::pRS303-CUP1pro-ATG39-mCherry*
YOT62	BY4741 *atg39Δ::natNT2 atg1Δ::zeoNT3 his3::pRS303-CUP1pro-ATG39$^{1-296}$-mCherry*
YOT37	BY4741 *natNT2-CUP1pro-ATG39-mCherry-hphNT1 TAL1-EGFP-zeoNT3 atg1Δ::URA3*
YOT38	BY4741 *natNT2-CUP1pro-ATG39-mCherry-hphNT1 NOP56-EGFP-zeoNT3 atg1Δ::URA3*
YOT22	BY4741 *natNT2-CUP1pro-ATG39-mCherry-hphNT1 HTA2-EGFP-kanMX6 atg1Δ::URA3*
YKM1512	BY4741 *natNT2-CUP1pro-ATG39-mCherry-hphNT1 TAL1-EGFP-kanMX6 ypt7Δ::zeoNT3*
YKM1506	BY4741 *natNT2-CUP1pro-ATG39-mCherry-hphNT1 HTA2-EGFP-kanMX6 ypt7Δ::zeoNT3*
YKM1515	BY4741 *natNT2-CUP1pro-ATG39-mCherry-hphNT1 HTZ1-EGFP-kanMX6 ypt7Δ::zeoNT3*
YKM1809	BY4741 *natNT2-HRR25pro-ATG39-EGFP-kanMX6 PUS1-mCherry-hphNT1*
YKM1813	BY4741 *natNT2-HRR25pro-ATG39$^{136-398}$-EGFP-kanMX6 PUS1-mCherry-hphNT1*
YKM1814	BY4741 *natNT2-HRR25pro-ATG39$^{167-398}$-EGFP-kanMX6 PUS1-mCherry-hphNT1*
YKM1857	BY4741 *natNT2-HRR25pro-ATG39$^{167-398}$-EGFP-kanMX6 OSW5-mCherry-hphNT1*
YKM2040	BY4741 *natNT2-HRR25pro-ATG39-mCherry-hphNT1 his3::mNeonGreen-ATG8-kanMX4 atg1Δ::zeoNT3*
YKM2041	BY4741 *natNT2-HRR25pro-ATG39-mCherry-hphNT1 his3::mNeonGreen-ATG8-kanMX4 atg2Δ::zeoNT3*
YKM2036	BY4741 *natNT2-HRR25pro-ATG39-mCherry-hphNT1 his3::mNeonGreen-ATG8-kanMX4 atg11Δ::zeoNT3*
YKM2043	BY4741 *natNT2-HRR25pro-ATG39-mCherry-hphNT1 his3::mNeonGreen-ATG8-kanMX4 atg11Δ::zeoNT3 atg17Δ::CgHIS3*
YOT43	BY4741 *natNT2-CUP1pro-ATG39-mCherry-hphNT1 HEH1-EGFP-kanMX4 atg1Δ::URA3 atg8Δ::zeoNT3*
YOT44	BY4741 *natNT2-CUP1pro-ATG39-mCherry-hphNT1 HEH1-EGFP-kanMX4 atg1Δ::URA3 atg11Δ::zeoNT3*
YKM1990	BY4741 *ATG39-mCherry-hphNT his3::pRS303-HRR25pro-mTurquoise2-HEH1$^{163-480}$*
YKM1138	BY4741 *natNT2-CUP1pro-ATG39-mCherry-hphNT1 ypt7Δ::zeoNT3*

Table S2. Plasmids used in this study

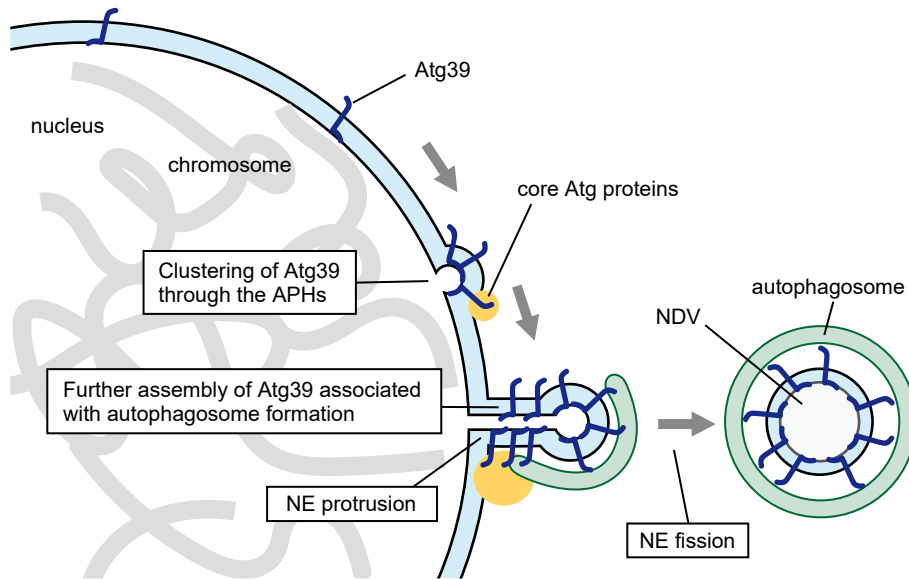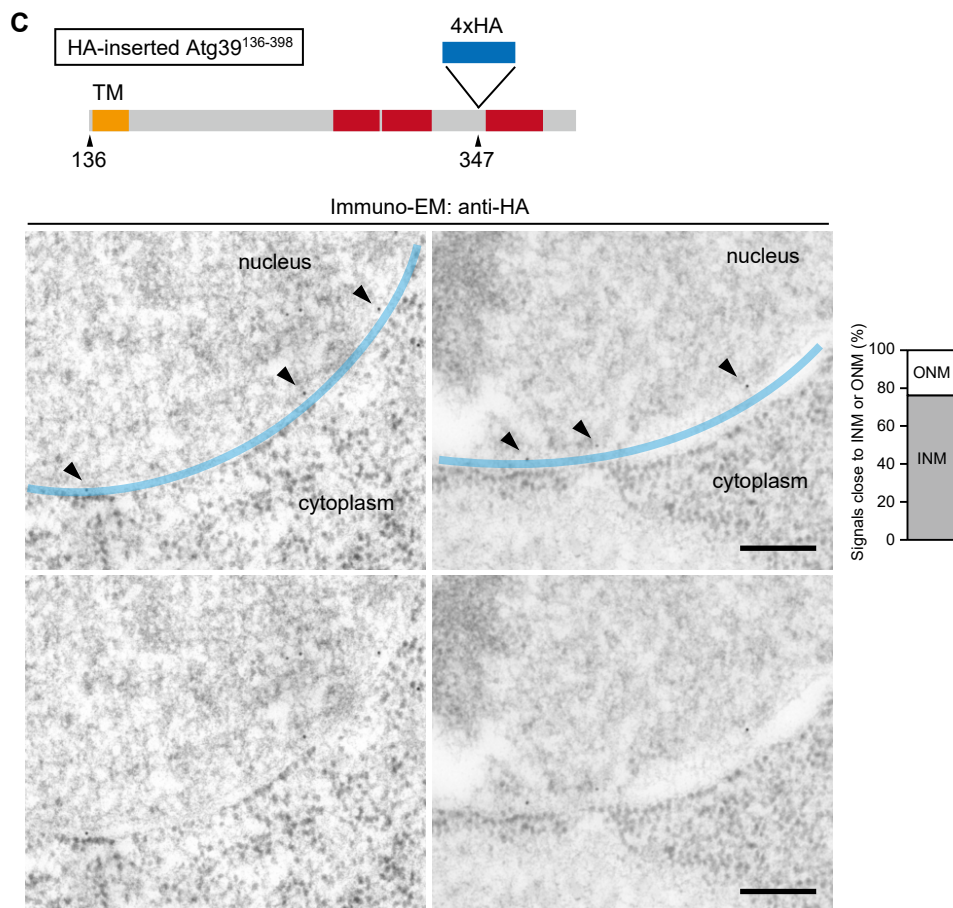| Name	Description
pKE453	pRS315–*NOP1pro-GFP$^{1-10}$-mCherry-PUS1*
pKE454	pRS315-*NOP1pro-GFP$^{1-10}$-mCherry-SCS2TM*
pKE386	pRS316-*HRR25pro-ATG39-2×mCherry*
pKE394	pRS316-*HRR25pro-ATG39$^{1-347}$-2×mCherry*
pKE465	pRS316-*HRR25pro-ATG39$^{1-325}$-2×mCherry*
pKE396	pRS316-*HRR25pro-ATG39$^{1-296}$-2×mCherry*
pKE398	pRS316-*HRR25pro-ATG39$^{1-194}$-2×mCherry*
pKE474	pRS316-*HRR25pro-ATG39$^{1-325\ 9A}$-2×mCherry*
pKE319	pRS316-*ATG39-6HA*
pKE475	pRS316-*ATG39$^{1-347}$-6HA*
pKE471	pRS316-*ATG39$^{1-325}$-6HA*
pKE480	pRS316-*ATG39$^{1-296}$-6HA*
pKE481	pRS316-*ATG39$^{1-194}$-6HA*
pKE487	pRS316-*HRR25pro-mTurquoise2-HEH1$^{1-480}$*
pKE497	pRS316-*HRR25pro-6FLAG-ATG39$^{136-347}$-4HA-ATG39$^{348-398}$-2×mCherry*

Figure 1
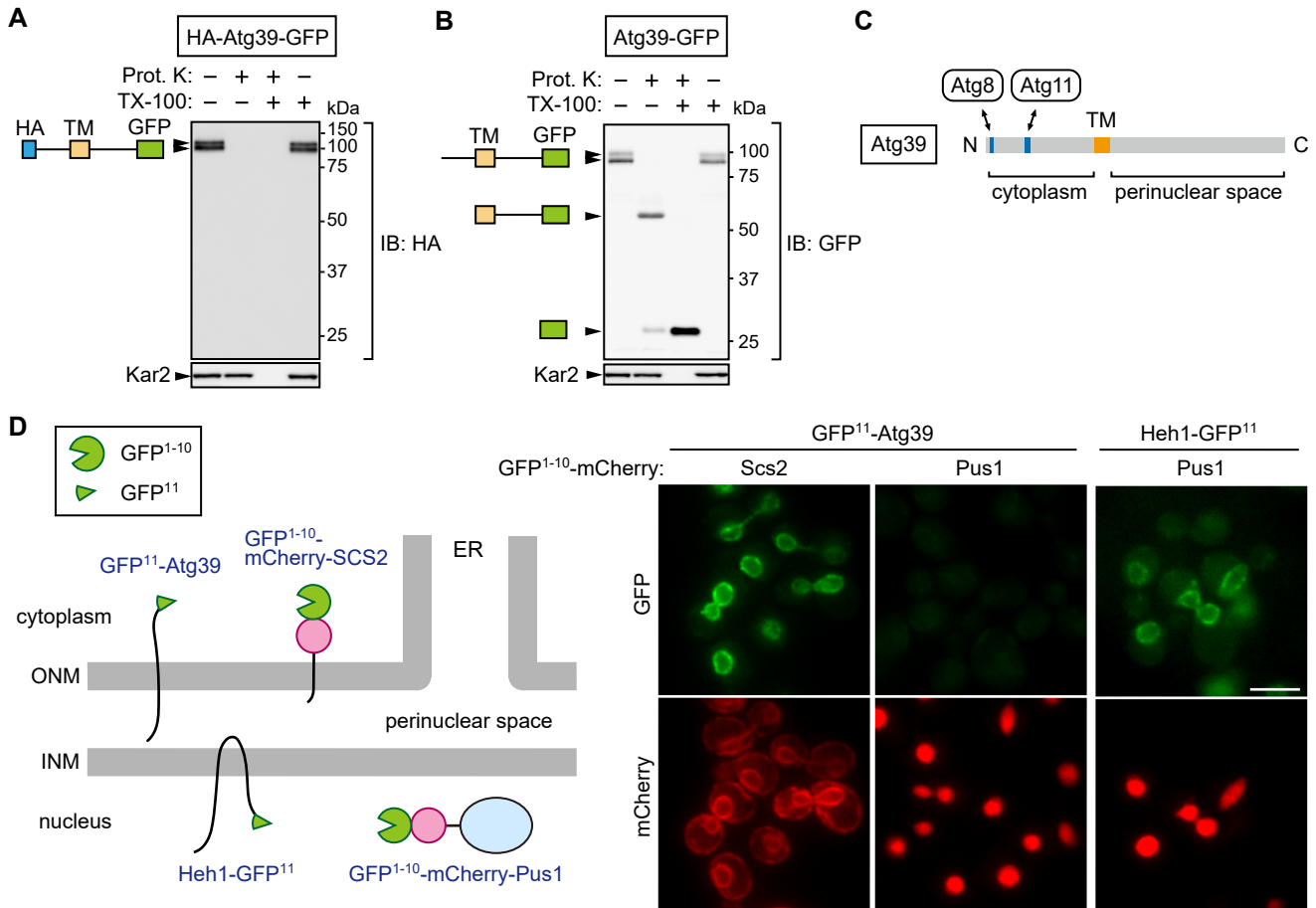
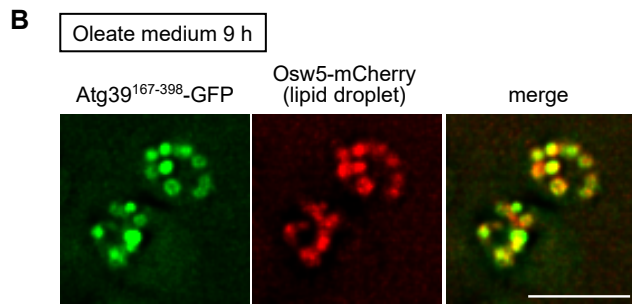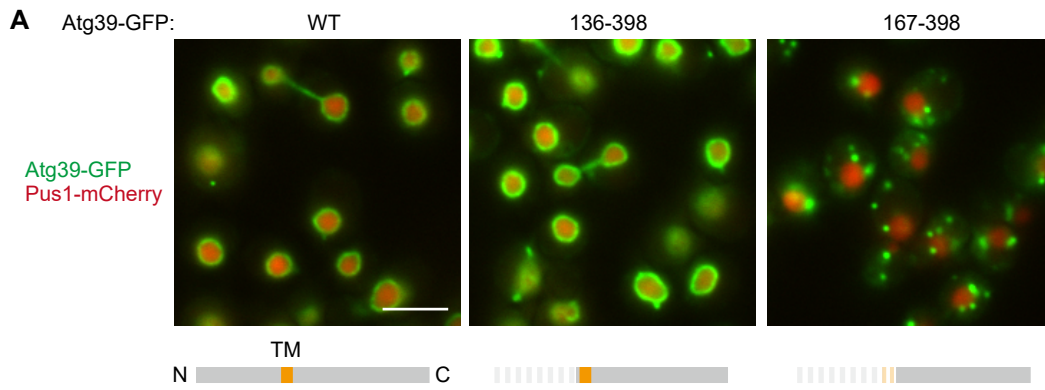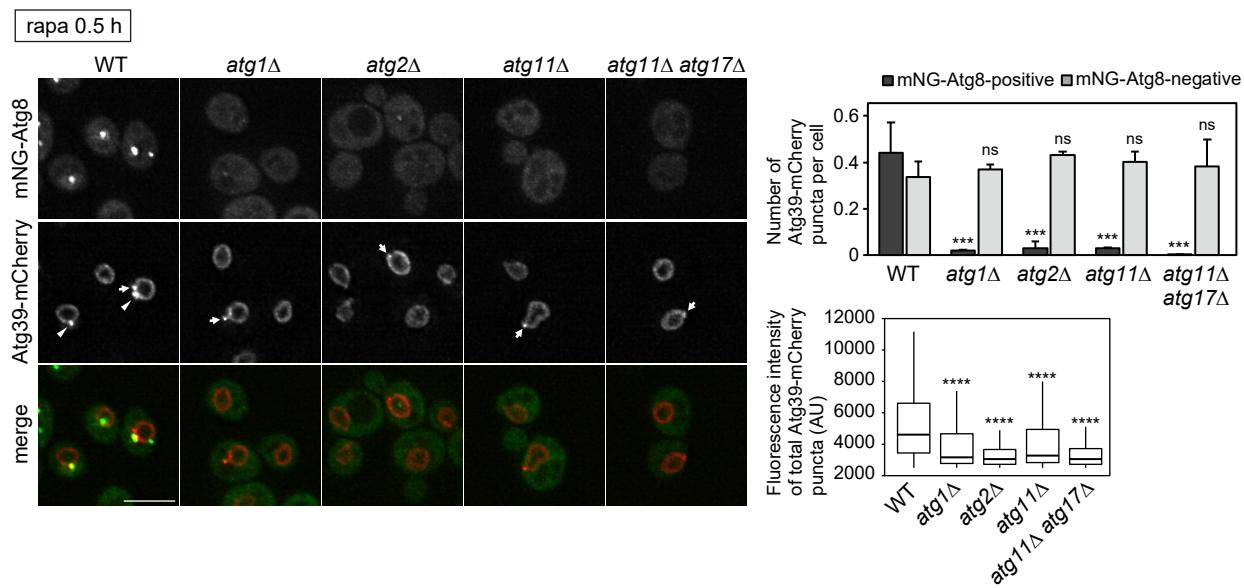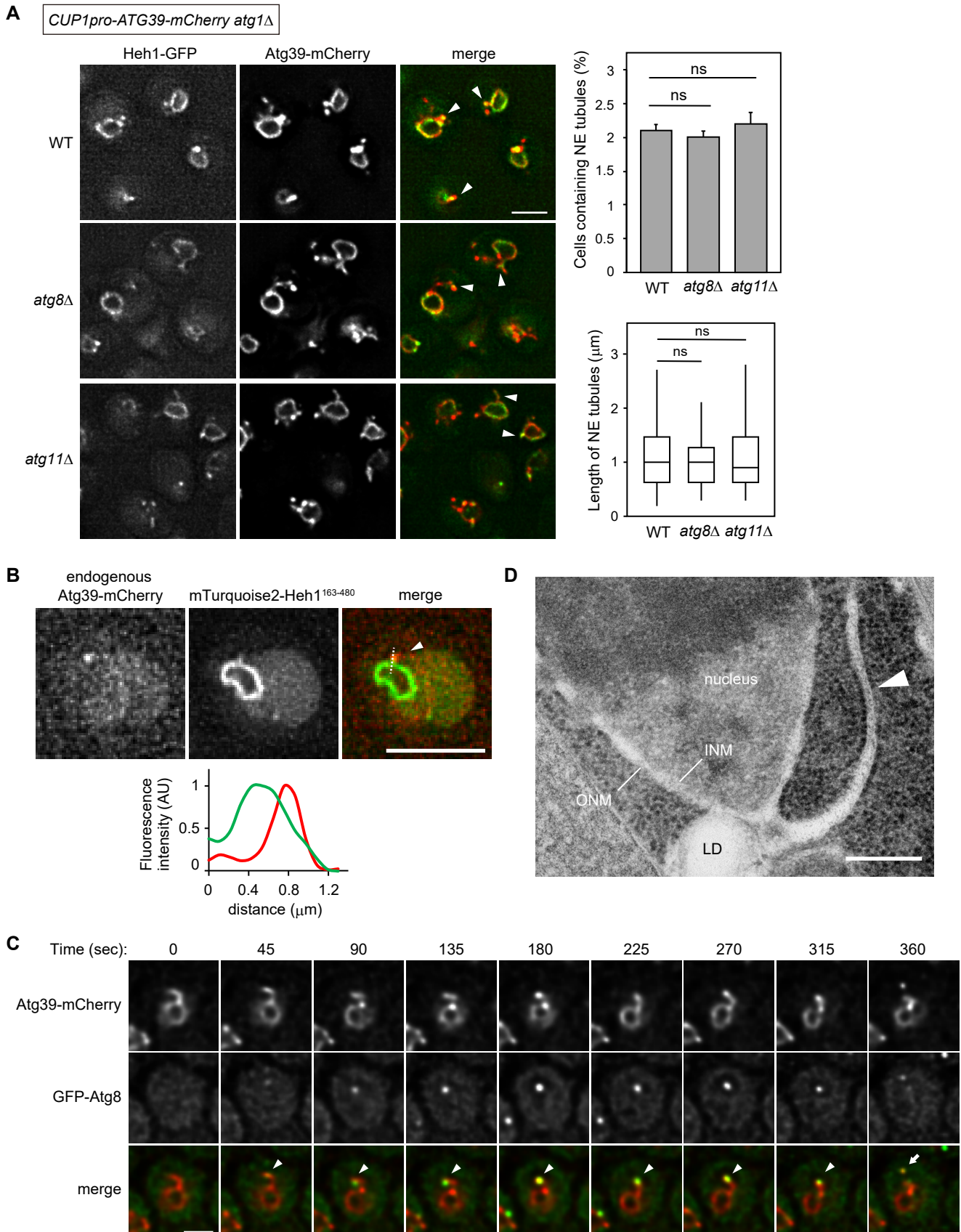**Figure 2**

Figure 3

Figure 4

A

B

C
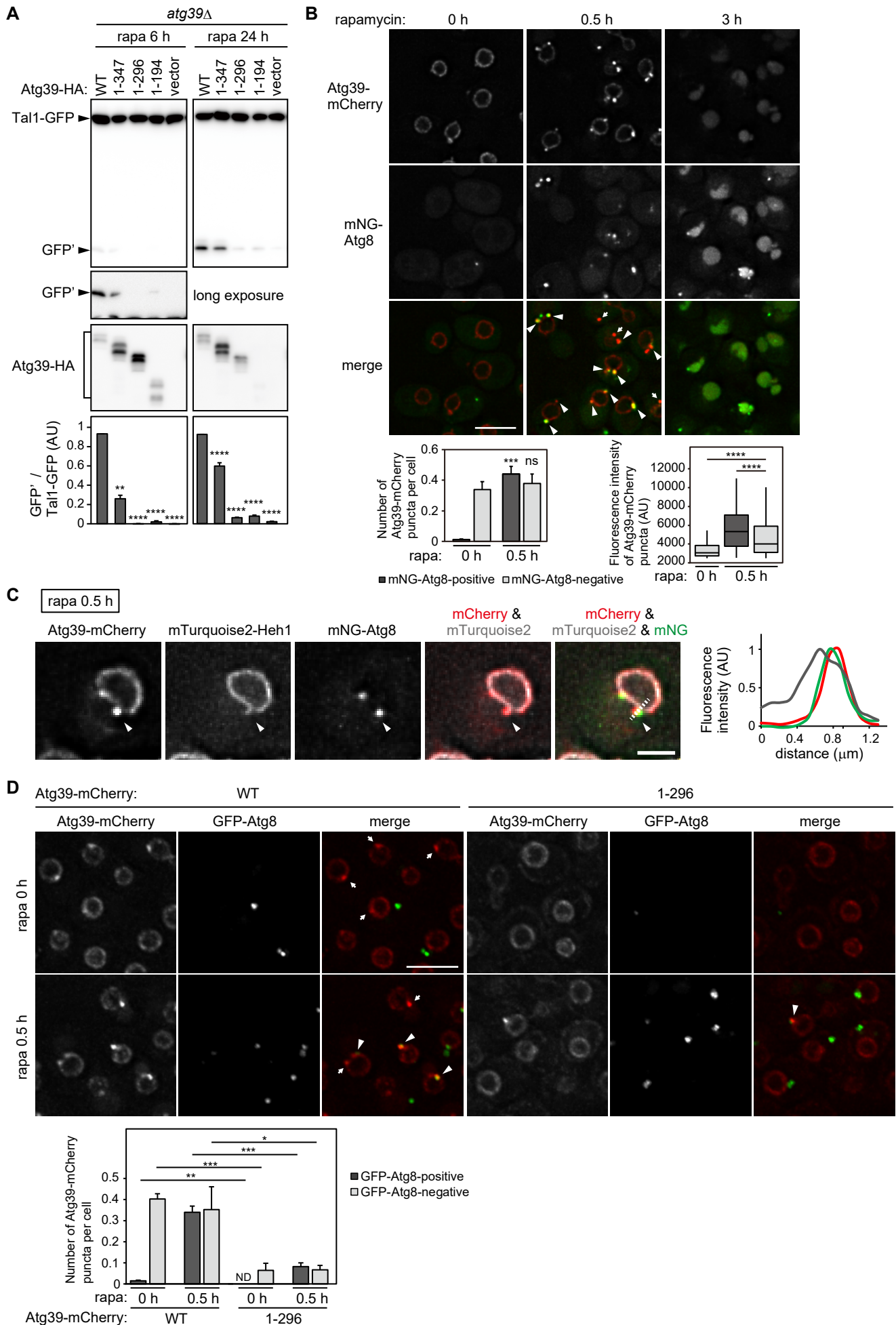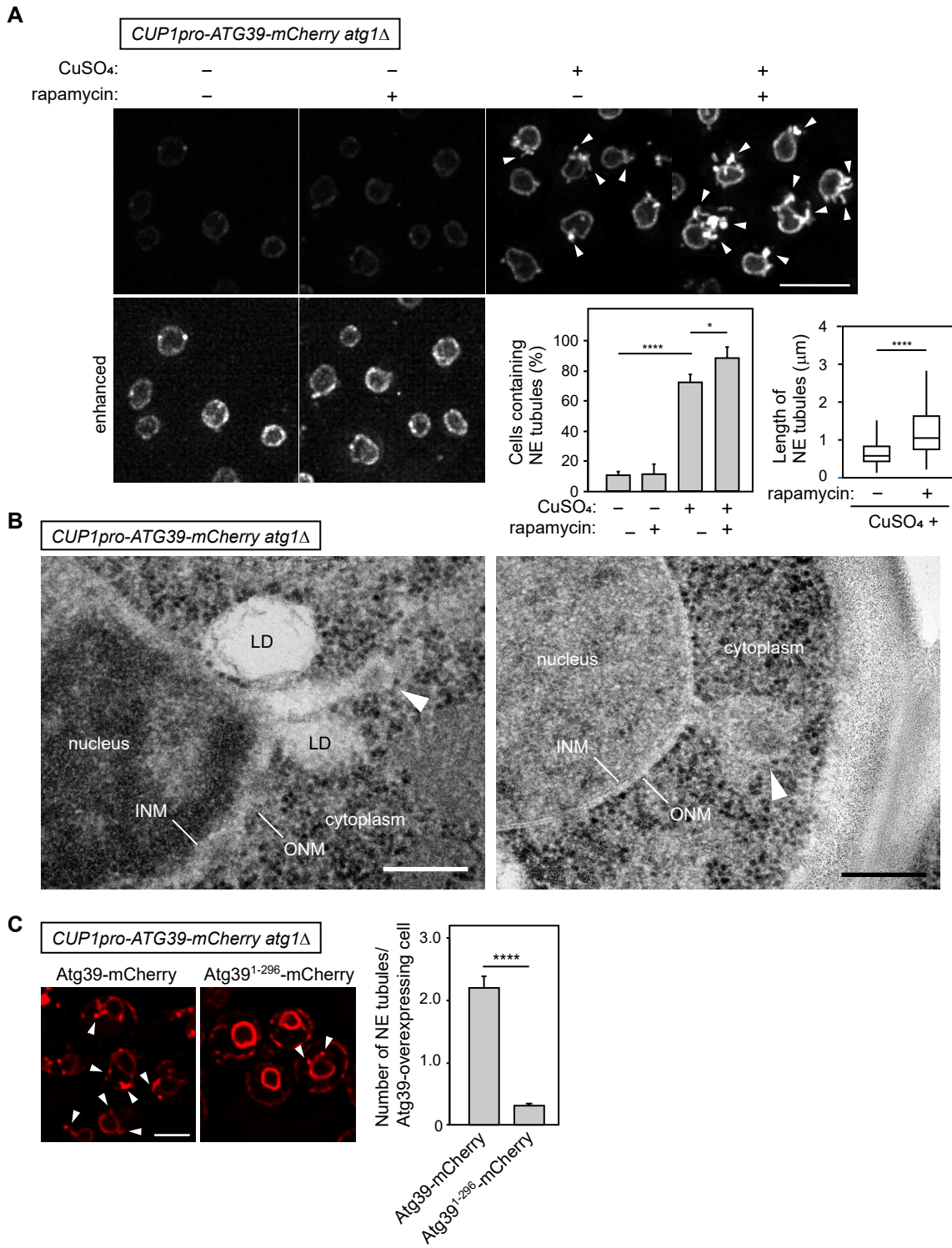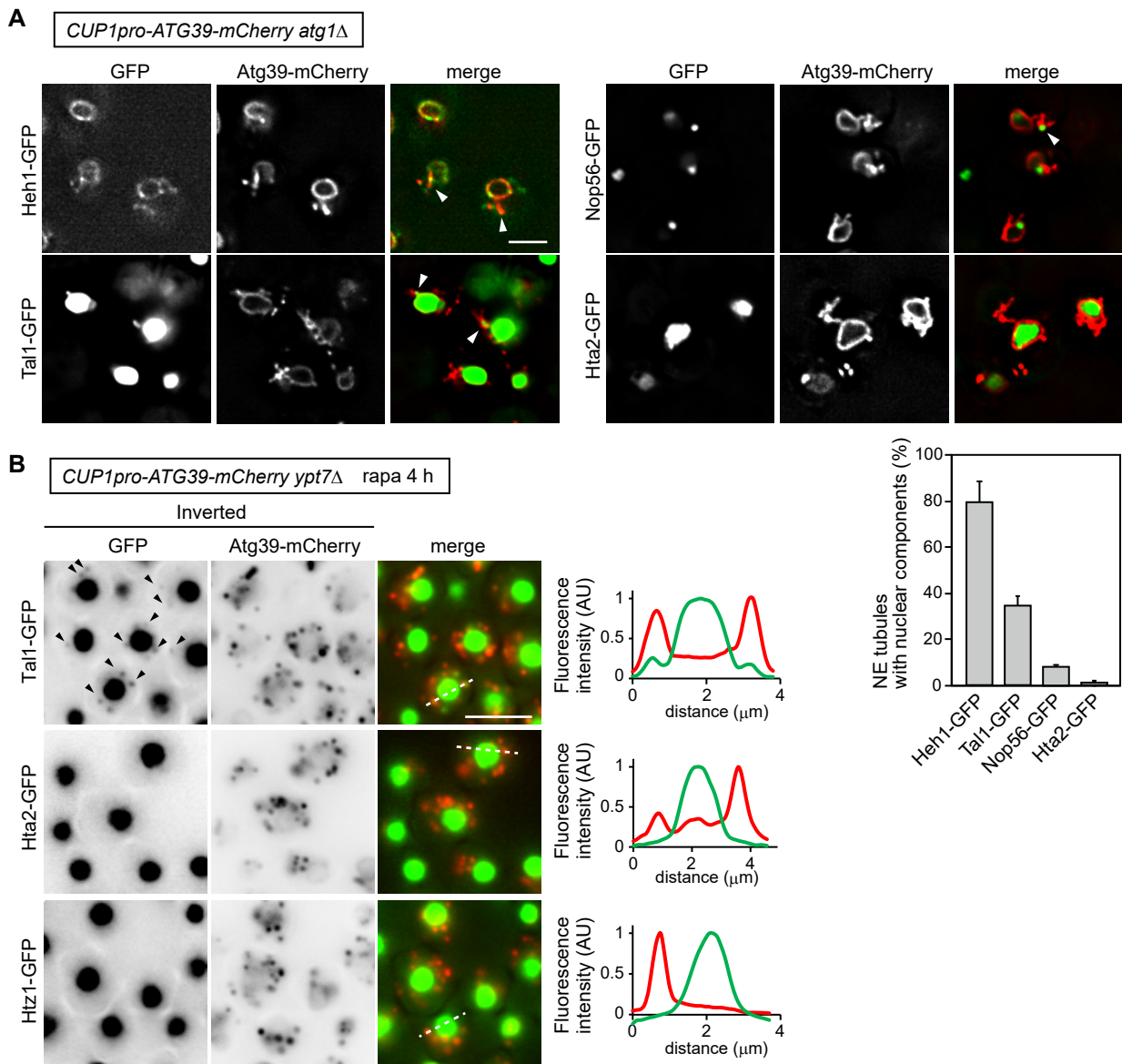
Figure 5

Figure 6

Figure S1

Figure S2

Figure S3

A

CUP1pro-ATG39-mCherry atg1Δ

B

D

C

Figure S4